

Effects of oxidation and impurities in lithium surfaces on the emitting wall plasma sheath

Kolter Bradshaw,¹ Ammar Hakim,² and Bhuvana Srinivasan³

¹Princeton University Department of Astrophysical Sciences, Princeton, NJ 08544, USA

²Princeton Plasma Physics Laboratory, Princeton, NJ 08543, USA

³University of Washington, Seattle, WA 98195, USA

(*Electronic mail: srinbhu@uw.edu)

(*Electronic mail: ahakim@pppl.gov)

(*Electronic mail: kb8689@princeton.edu)

(Dated: 30 January 2025)

Use of lithium as a surface coating in fusion devices improves plasma performance, but the change in wall properties affects the secondary electron emission properties of the material. Lithium oxidizes easily, which drives the emission yield well above unity. We present here simulations demonstrating the change in sheath structure from monotonic to the nonmonotonic space-charge limited sheath using an energy-dependent data-driven emission model which self-consistently captures both secondary emission and backscattering populations. Increased secondary electron emission from the material has ramifications for the degradation and erosion of the wall. Results shows that the oxidation leads to an increased electron flux into the wall, and a reduced ion flux. The net transfer of energy to the surface is significantly greater for the oxidized case than for the pure lithium case. High reflection rates of low-energy backscattered particles leads to a high re-emission rate at the wall.

I. INTRODUCTION

In plasma devices, such as the tokamak¹ and Hall thrusters,² where plasma is constrained to flow within a channel, the interaction between the confined plasma and the material surface of the device plays a decisive role in both plasma performance and the durability of the device. High particle fluxes to the wall can lead to high rates of ion recycling, which degrades plasma performance, while erosion of wall material degrades durability and increases the potential of catastrophic device failure. The plasma sheath³ plays a key role in shielding the wall from high electron fluxes, though it accelerates ions and increases recycling rates. Emission of electrons from the surface into the sheath reduces this shielding by decreasing the wall potential,⁴ providing better protection from ion impact, but allowing higher electron fluxes into the wall. Application of liquid metal films, such as lithium, have seen increased use in recent years^{5–8} due to their high binding rate with hydrogen, reducing fuel recycling and increasing plasma performance.⁹ However, while lithium has a low emission rate when pure, it oxidizes easily and begins to emit at much higher rates.^{10,11} The level of exposure required for this oxidation to occur is commonly experienced in fusion devices,¹² making it an important consideration for any plasma-surface interactions. Understanding the ramifications this may have on wall durability requires a thorough understanding of how the plasma sheath responds to this strong emission.

The classical sheath maintains a flux balance at the material surface by accelerating ions and retarding the more mobile electrons. The presence of electron emission adds an outbound flux at the wall, altering the flux balance kept by the sheath,

$$\Gamma_{pe} = \Gamma_{se} + \Gamma_i. \quad (1)$$

Here, the incoming electron flux from the bulk plasma (Γ_{pe}) is

balanced by the total ion flux (Γ_i) and the outgoing secondary electron flux away from the wall (Γ_{se}). We define the parameter $\gamma = \Gamma_{se}/\Gamma_{pe}$, to denote the *secondary electron emission coefficient*, or the ratio of emitted flux at the wall to incoming flux from the bulk plasma.

The addition of this outbound flux leads to a drop in wall potential as less of a barrier is required to balance Eq. 1. Hobbs & Wesson⁴ describe this decay in the sheath with increasing Γ_{se} , culminating with the flux ratio reaching some critical value γ_c , where the monotonic sheath is no longer capable of balancing the fluxes and a barrier must form close to the wall to reflect back some portion of Γ_{se} , denoted as Γ_{ref} . Noting that by definition $\Gamma_{se} = \gamma\Gamma_{pe}$, the resulting flux balance becomes

$$\Gamma_{pe}(1 - \gamma) + \Gamma_{ref} = \Gamma_i. \quad (2)$$

This indicates the formation of the so-called space-charge limited (SCL) sheath, with a non-monotonic potential dip near the wall.⁴ If γ grows to exceed unity, the Γ_{pe} term becomes negative. Here, two solutions are possible. As before, an SCL is capable of providing sufficient Γ_{ref} to maintain the flux balance. However, it is also possible for the polarity of the sheath to reverse entirely with the formation of an inverse sheath, where the wall potential is positive relative to the sheath entrance, electrons are accelerated, and ions are decelerated.¹³ The work done by Campanell & Umansky^{14,15} demonstrates that the inverse sheath mode is preferred for all $\gamma > 1$ in the presence of ion-neutral collisional effects, which lead to an accumulation of cold ions in the potential dip of the SCL and drive the transition. Without some source of cold ions, the sheath will remain in the SCL state for all $\gamma > \gamma_c$.

Building on past sheath work,^{16–18} this paper explores the effect of lithium oxidation on the plasma sheath. The purpose is to examine key properties of the emitting sheath with an eye to how they may impact durability of the wall mate-

rial. Section II discusses the numerical model and treatment of secondary electron emission. Particular attention is given to the estimation of emission behavior in the low energy regime from secondary electron yield data. Simulations are set up in Section III giving comparisons of clean and oxidized lithium parameters. Section IV gives a discussion of the results, with an emphasis on how the different emission properties modify the overall sheath structure and energy fluxes into the wall.

II. MODEL

A. Discrete Kinetic Equations

The simulation work shown in this paper is produced by the Gkeyll software,¹⁹ using the continuum kinetic approach of applying the discontinuous Galerkin (DG) numerical method²⁰ to evolve the Vlasov-Poisson system of equations,^{21,22} consisting of the electrostatic Boltzmann equation

$$\frac{\partial f_s}{\partial t} + \mathbf{v} \cdot \nabla_{\mathbf{x}} f_s + \frac{q_s}{m_s} \mathbf{E} \cdot \nabla_{\mathbf{v}} f_s = \left(\frac{\partial f}{\partial t} \right)_c + S_{src}, \quad (3)$$

coupled with Poisson's equation through the electric field.

The collision term is a Bhatnagar-Gross-Krook (BGK) operator, used to thermalize the presheath plasma. It takes the form

$$\left(\frac{\partial f_s}{\partial t} \right)_c = \nu_s \left(\frac{n}{n_0} f_{0,s} - f_s \right), \quad (4)$$

where n_0 is the initial density and ν_s is the collision frequency. This relaxes the distribution towards $f_{0,s}$, the Maxwellian distribution at the initial temperature T_0 . Temperature is fixed for the collision operator as otherwise losses of energetic electrons to the wall will cause a steady cooling over time, preventing a steady state presheath temperature from developing. Previous work has studied the effects of collisions on the Bohm criterion.^{23,24} To prevent the thermalization from extending into the sheath region, which is physically close to collisionless, the collision frequency follows a spatial profile

$$\nu_s(x) = \frac{\nu_{0,s}}{1 + \exp\left(\frac{|x|}{3\lambda_D} - \frac{16}{3}\right)}, \quad (5)$$

which falls off quickly towards zero at around $\approx 40\lambda_D$ from the presheath domain boundary, with $\lambda_D = \sqrt{\frac{\epsilon_0 T_0}{n_0 q_0^2}}$ being the Debye length.

A source term S_{src} is also used to preserve the particle balance,

$$S_{src} = \frac{\Gamma_i^+}{L_{src}} \left(\frac{2(L_{src} - |x|)}{L_{src}} \right) \frac{n}{n_0} f_{0,s}. \quad (6)$$

For both species, the ion flux into the wall Γ_i^+ is used to preserve quasineutrality. $L_{src} = 40\lambda_D$ is the source length, over which there is a linear decreasing profile. This source region,

which includes both the area of particle introduction and high collisions, exists to artificially create a region from which thermal particles will flow into the presheath and replenish particle losses to the wall. The addition of particles in this region will create a non-physical "source sheath"²⁵ at the presheath edge.

B. Emission Yield Fits to Material Data

There are two primary modes of electron emission which are expected to occur at the material surface.²⁶ Some electrons which impact the surface either lack the energy to penetrate and are reflected elastically, or penetrate but are re-emitted after several scattering events internal to the material while losing some energy. These are the "backscattered" electrons. The true "secondary" electrons are emitted directly from the material in response to electron impact. The total ratio of impacting to emitted particles is defined here as the *secondary electron yield* δ . This is distinguished from the SEE coefficient γ by being the full flux ratio at the wall $\delta = \Gamma_{se}/(\Gamma_{ref} + \Gamma_{pe})$, while γ neglects the reflected electron population and is more characteristic of the flux ratio using the incoming flux measured at the potential minimum. For a classical sheath where there is no potential barrier reflecting emitted electrons back to the wall, γ and δ are equivalent.

Data from Bruining & De Boer¹⁰ (reproduced in Fig. 1) shows results for both "pure" and "impure" lithium values of δ , with the measured yields being significantly higher in the impure case. Thorough measurements of the electron yield for different oxidized samples of lithium from Capece et al¹¹ reinforce the choice of the Bruining & De Boer data as a good upper limit for the emission in cases of high lithium impurity.

In order to rigorously fit secondary electron emission models to this data, both backscattering and secondary emission processes must be considered. Ideally, the overall yield curve would be decomposed based on the emission spectrum, where clear distinctions can generally be made on which particles were elastically reflected on impact, and which are "true" secondary electrons. This data is not present in the literature for lithium, so informed estimates must be made based solely on the yield curve. Noting that elastic backscattering is generally negligible at high energy and rises at low energy,²⁷ the simplest way of separating the two contributions is to fit the yield curve to the high energy data, and watch for an undershoot at low energy where the backscattering is not being accounted for, fitting to that undershoot for the elastically reflected particles.

There is still some ambiguity in the literature around what low energy emission behavior should look like. The work of Cimino et al^{28,29} suggests that it is common to see a rise in the emission yield towards unity as energy goes to zero. The accuracy of this has been questioned in light of past experiments,³⁰ but in a follow-up paper³¹ on measurements of the yield for copper, Cimino et al observed that the rise appears to be physical for the impure, "as-received" material samples, while the clean samples are more consistent with previous literature³²⁻³⁴ showing a decline towards zero of the

yield at low energy.

The fitting model for the true secondary electron yield δ_{ts} comes from Furman & Pivi,²⁷

$$\delta_{ts}(E', \mu') = \hat{\delta}(\mu')D(E'/\hat{E}(\mu')), \quad (7)$$

$$\hat{\delta}(\mu') = \hat{\delta}_{ts}[1 + t_1(1 - \mu'^{t_2})], \quad (8)$$

$$\hat{E} = \hat{E}_{ts}[1 + t_3(1 - \mu'^{t_4})], \quad (9)$$

$$D(x) = \frac{sx}{s - 1 + x^s}, \quad (10)$$

where \hat{E}_{ts} , $\hat{\delta}_{ts}$, t_1 , t_2 , t_3 , t_4 and s are fitting parameters, with \hat{E}_{ts} and $\hat{\delta}_{ts}$ corresponding to the energy of maximum yield and maximum yield, respectively. The fit is done specifically to the high energy peak region of the data, where the bulk of the emission should be from secondary electron emission.

The true secondary emission yield fits to the lithium data in Fig. 1 suggest similar behavior as to that observed by Cimino et al for copper.³¹ The fit to the peak of the impure lithium measurements exhibits a distinct undershoot of the yield that increases with decreasing energy despite excellent correlation at high energy, suggesting a rise in the yield due to backscattering at low energy. Conversely, while the data is too sparse at low energies for full confidence, a similar fit suggests no such upward trend occurs in the clean lithium data.

To account for the apparent increase in yield at low energy in the oxidized data, a second fit is done to low energy using the model developed by Cazaux³⁵ to estimate the backscattering yield δ_r ,

$$\begin{aligned} E_s &= E' + E_f + \phi_r \\ G &= 1 + \frac{E_s - E'}{E' \mu'^2}, \\ \delta_r(E') &= \frac{(1 - \sqrt{G})^2}{(1 + \sqrt{G})^2}, \end{aligned} \quad (11)$$

where E_f and ϕ_r are fitting parameters identified with the Fermi energy and work function of the material, respectively. No second fit is required for the clean data as the initial fit matched the data well across the entire energy range. The resulting parameters for both the elastic and inelastic fits are shown in Table I

Inelastic backscattering is typically approximately constant at high energies,²⁷ and is therefore folded into the secondary emission instead of being represented separately. As backscattering is directly related to the atomic number Z , it is estimated to be quite low at high energy in any event for a low Z material like lithium.³⁶

C. Boundary Condition

The emission is implemented as a boundary condition where the inelastic and elastic populations are fully

Lithium	\hat{E}_{ts}	$\hat{\delta}_{ts}$	t_1	t_2	t_3	t_4	s	E_f	ϕ_r
Clean	97.18	0.567	0.66	0.8	0.7	1.0	1.42	0	0
Oxidized	354.52	4.208	0.66	0.8	0.7	1.0	1.79	290.31	144.49

TABLE I. Fitting parameters for oxidized and clean boundary condition. The clean case has negligible elastic emission, so those parameters are set to zero.

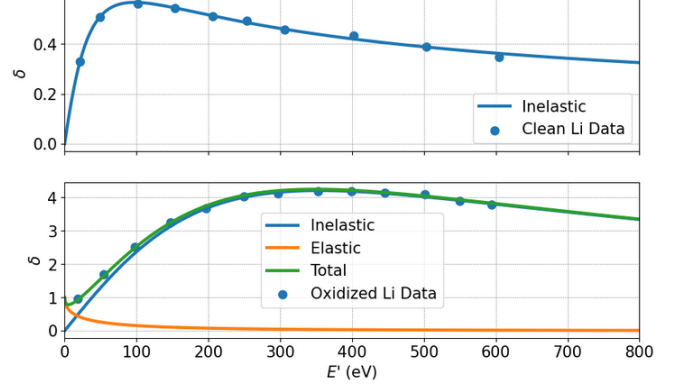


FIG. 1. Yield data from Bruining & De Boer¹⁰ for clean (top) and impure (bottom) lithium, with fits to the elastic and inelastic regions of the yield. A fit to the peak of the impure lithium curve results in an increasing undershoot of the emission at low energies, suggesting a rising elastic backscattering coefficient at low energy. This trait is not evident in the sparse clean lithium data, suggesting negligible backscattering at low energy. Figure taken from a Ph.D. dissertation.³⁷

modeled.¹⁸ The boundary condition sets the distribution function in a layer of “ghost” cells outside the domain edge, which are used in the numerical update of the interior “skin” cells neighboring the material wall. Taking $+$ to denote the incoming direction into the wall, and $-$ the outgoing direction away from the wall, the result is the ghost cell distribution being set to

$$f_e^{g-}(\mathbf{x}, \mathbf{v}) = f_r(\mathbf{x}, \mathbf{v}) + C_{ts}f_{ts}(\mathbf{v}), \quad (12)$$

where f_r is the distribution of elastically reflected particles, f_{ts} is the distribution of emitted secondary electrons, and C_{ts} is the normalization factor which sets the correct flux ratio between the emitted and impacting electrons. The elastic distribution is found by simply scaling the incoming distribution in the skin cell by the elastic yield,

$$f_r(\mathbf{x}, \mathbf{v}) = \delta_r(\mathbf{v})f_e^{s+}(\mathbf{x}^-, \mathbf{v}^-), \quad (13)$$

where the coordinates \mathbf{x}^- , \mathbf{v}^- indicate a transformation from incoming to outgoing coordinates (i.e., $\mathbf{x}^-, \mathbf{v}^- = (-x, y, z), (-v_x, v_y, v_z)$ at the x -boundary). Since there is no complete data available for the energetic distribution of secondary electrons for lithium, it is best estimated using the theory from Chung & Everhart³⁸

$$f_{ts}(\mathbf{v}) = \frac{E(\mathbf{v})}{(E(\mathbf{v}) + \phi)^4}, \quad (14)$$

where φ , the material work function, is the sole material parameter dependence. For lithium, this value is $\varphi \approx 3 \text{ eV}$.³⁹ The Chung-Everhart model places the energy at which the peak of the emitted distribution is located at $\varphi/3 = 1 \text{ eV}$. For the Chung-Everhart spectrum, the normalization factor is calculated to be

$$C_{ts} = \frac{6m_e}{q_0} \varphi^2 \bar{\delta}_{ts} \Gamma_e^+, \quad (15)$$

where $\bar{\delta}_{ts}$ is the weighted average of the secondary electron yield over the incoming velocity space,

$$\bar{\delta}_{ts} = \frac{\sum_{j=1}^{N_v^+} \Gamma_e^j \delta_{ts}(v_c^j)}{\Gamma_e^+}. \quad (16)$$

Here, Γ_e^j is the electron flux of the distribution function into the boundary cell j , and v_c^j is the cell center velocity.

III. SIMULATIONS

The choice of 1X1V domain is $N_x = 960$ cells in configuration space, with bounds of $[0, 128\lambda_D]$. In velocity space, there are $N_v = 512$ cells with bounds of $[-4v_{t,e}, 4v_{t,e}]$ for the electrons, and $[-6v_{t,i}, 6v_{t,i}]$ for the ions, where $v_{t,s} = \sqrt{\frac{T_0}{m_s}}$ is the thermal velocity of the particle species. The plasma is initialized to a uniform temperature of $T_0 = 150 \text{ eV}$ for both electrons and ions. The initial density is $n_0 = 1.0 \times 10^{16} \text{ m}^{-3}$. The source length is $L_s = 40\lambda_D$.

Three different cases are presented here, distinct by choice of material fit and collisionality. Case 1 uses the clean lithium boundary parameters, and a high collisionality of $\bar{v}_{0,s} = v_{0,s}\lambda_D/v_{t,s} = 0.2$. Case 2 uses the same high collisionality with oxidized lithium parameters. Case 3 is oxidized, with the marginally collisional $\bar{v}_{0,s} = 0.02$. This final case is included to demonstrate possible behavior when turbulence propagates into the sheath region, whether as a result of turbulent activity in the core plasma or due to emitted beams propagating from the other wall such as might occur in a narrow channel application (such as the Hall thruster).

If emission is applied at full strength immediately to the uniform plasma, it triggers the sudden introduction of a sharp density gradient within the domain edge cell due to the large number of energetic particles being allowed to reach the wall and emit. This can cause serious positivity issues, so for these simulations the boundary condition is set to increase from zero emission at $t\omega_{pe} = 0$ to full emission at $t_b\omega_{pe} = 1000$. This is done by scaling the normalization factor for the emitted distribution by a factor of $\sin(\frac{\pi t}{2t_b})$ for $t < t_b$. This allows the plasma to relax from the initial uniform condition to the sheath where fewer high energy particles are present without compromising the stability of the simulation.

There is no mechanism present in the simulations to provide cold ions in the sheath region to drive a potential transition to an inverse sheath. Neutral effects are currently not implemented extensively in the Vlasov-Poisson code being used, and attempts to replicate the effects of similar processes on the

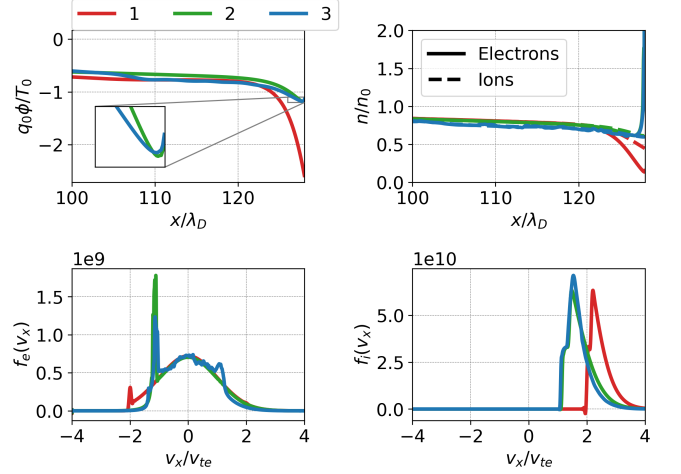


FIG. 2. Profiles for the potential, density, and species distribution functions at $t\omega_{pe} = 8000$ for clean lithium with strong collisions (1), oxidized lithium with strong collisions (2), and oxidized lithium with weak collisions (3). The electron distributions are averaged over the presheath from $60\lambda_D$ to $100\lambda_D$, while the ion distributions are taken at the wall boundary. The oxidized lithium cases form SCL sheaths, with high electron accumulation at the wall and higher intensity emitted beams are visible in the distribution. The marginally collisional case is noticeably less Maxwellian in the electron distribution, and the turbulence leads to a flattening of the center of the distribution, and a beam propagating back from the left boundary is visible. The clean case, which forms a classical sheath, accelerates ions more than the SCL cases due to the greater sheath potential drop.

ions using a non-physical extension of collisions or the source term into the sheath lead to inconclusive results. Accumulation of trapped ions and decreases in sheath potentials are observed, but none of these tests result in an inverse sheath transition on simulation time scales. Due to a lack of confidence in any conclusions on the expected long-term behavior of the sheath drawn from these simulations, they are omitted from this work.

Trapped ions can appear organically in the potential dip if the time relaxation is not used and full emission is permitted immediately. This occurs during the initial relaxation from the uniform state, where the potential dip forms rapidly enough to capture some portion of the cold ions before the ion distribution fully accelerates to higher speeds. In one previous simulation, this initial trapping is even seemingly enough to drive a reverse sheath transition,³⁷ though this only occurs in a single known case where the presheath temperature is not fixed and significant cooling across the simulation domain also occurs. In any case, this trapped population remains mostly static as no additional source is present, and does not represent a physically significant result.

IV. RESULTS

The cases with the impure lithium experience significantly higher emission, as predicted. Fig. 2 compares the sheath pro-

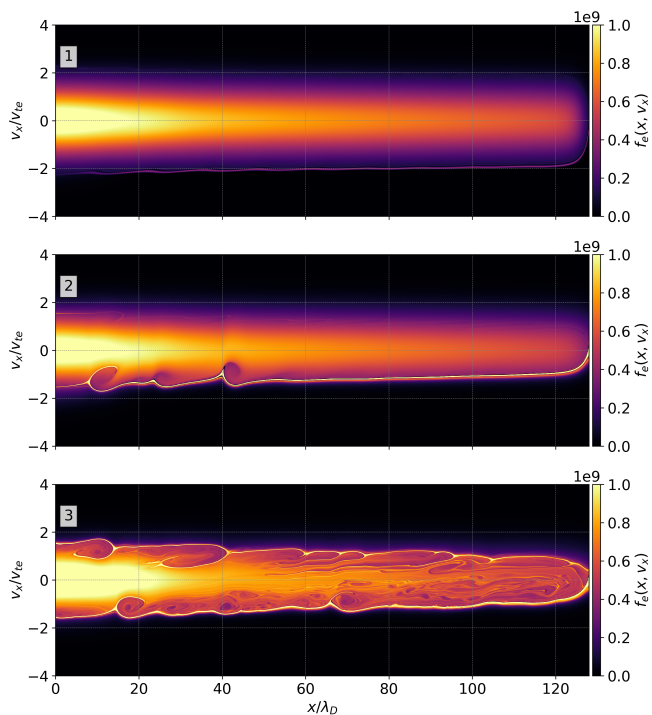


FIG. 3. Electron distribution function at $t\omega_{pe} = 8000$ for clean lithium with strong collisions (1), oxidized lithium with strong collisions (2), and oxidized lithium with weak collisions (3). Emission drives a beam of electrons from the wall which penetrates the presheath, exciting two-stream effects in cases of strong emission. The weakly collisional oxidized case experiences strong turbulence when these modes propagate back to the sheath.

files for each case. The clean lithium (case 1) produces classical sheath profiles for the potential and density. The two oxidized lithium cases both produce comparable SCL sheath profiles, with a non-monotonic potential and a sharp accumulation of electrons in the potential dip region. Ion density drops less sharply in the SCL than in the classical case. There is no cold ion trapping in the potential well, as expected.

Important quantities for the three cases are tabulated in Table II. Despite the high theoretical SEE yields predicted by the lithium data, δ_{tot} is rapidly driven to less than unity at the wall as the theory expects. Measured at the potential minimum, however, the flux ratio coefficient γ is significantly greater than unity for the oxidized cases. For the classical case, these two quantities are of course the same, and significantly less than unity.

Fig. 3 compares the electron distribution functions of the three cases. All three have a clear beam of emitted electrons proceeding from the surface, with the oxidized beams having a far greater density than in the clean lithium case. Additionally, the oxidized cases show this counterstreaming beam exciting a streaming instability as it is accelerated into the presheath. In case 2, this mode reaches the left boundary and is damped by the collisions there. In the marginally collisional case, these modes propagate back to the sheath region without being fully damped, and heavy turbulence is excited

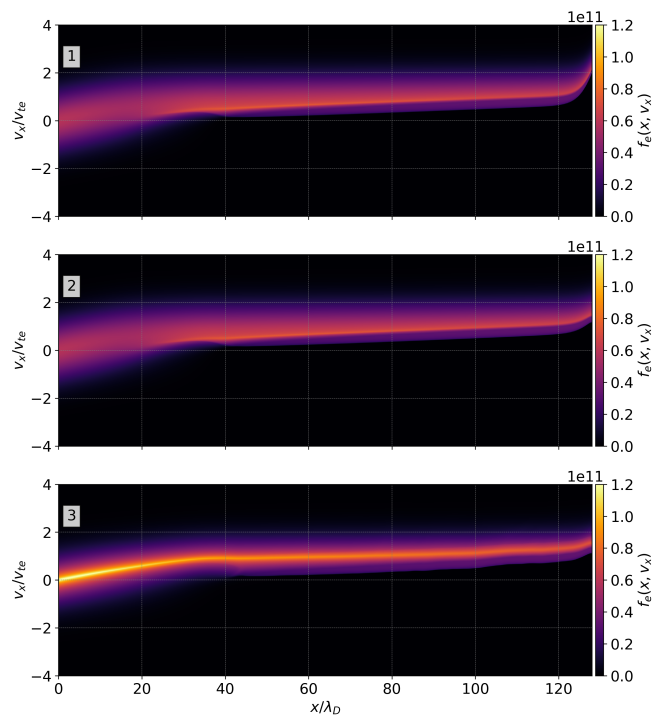


FIG. 4. Ion distribution function at $t\omega_{pe} = 8000$ for clean lithium with strong collisions (1), oxidized lithium with strong collisions (2), and oxidized lithium with weak collisions (3). Only the strongly collisional cases effectively thermalize the source region. The classical case accelerates ions at a greater rate than the SCL cases.

in the collisionless region. Fig. 4 shows the ion distributions. The marginally collisional case does not succeed in fully thermalizing the source ions, but the two highly collisional cases do. The clean lithium shows more acceleration occurring in the sheath region, as the potential drop is greater for the classical sheath profile than in the SCL sheath.

The mechanism by which δ_{tot} is driven to less than unity at the surface is clear by examining Fig. 5, which decomposes the component distributions of the impacting and emitted electrons late in time. In the oxidized case, backscattering has come to dominate over the true secondary electrons in the emitted distribution. An analysis of the SEE yield shows that in both of the oxidized lithium cases over 70% of the total emission flux is contributed by elastic backscattering, with the remaining 30% accounted for by the secondary electrons. This is only possible due to an accumulation of low-energy particles at the wall, as was noted when discussing the sheath density profiles. The SCL sheath potential barrier reflects some portion of emitted low-energy electrons back to the wall. Here, they collide and undergo a high rate of elastic backscattering, causing most of them to re-emit. This process repeats, further skewing the distribution towards lower energy and biasing it towards the elastic backscattering regime. This leads to a distribution that is primarily in the backscattering ($\delta_e \leq 1$ by definition) and low δ_{ts} region of the yield curve, driving the total yield below unity. In the classical sheath case, this skew does not occur and the distribution into the wall remains near

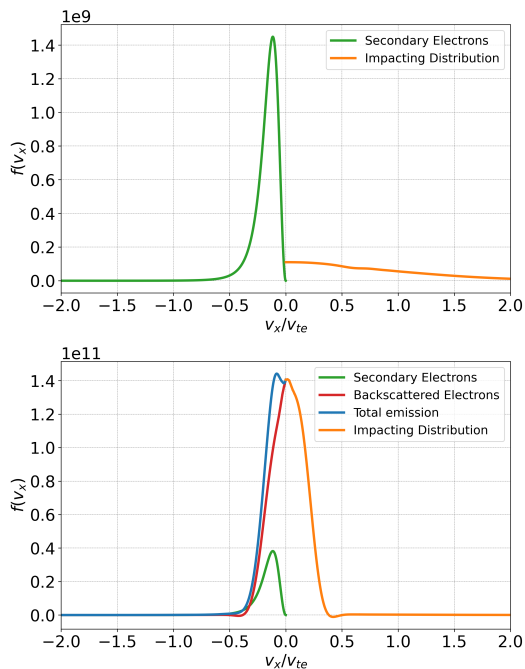


FIG. 5. Comparison of emitted distributions of electrons to the impacting electron distribution. In the clean case (top), only true secondary electron emission occurs, so there is only a single population following the Chung-Everhart distribution. For the oxidized case (bottom), the backscattered electrons grow to dominate over the secondary electrons. Note the different magnitudes between the two cases, and the lower average energy in the oxidized case. Low-energy backscattered particles are reflected back to the wall by the potential barrier in the SCL sheath, where they re-scatter and repeat the process, leading to the accumulation of low-energy electrons which drives the mean incident energy further towards the backscattering-dominant regime.

to a Maxwellian. The clean lithium has no backscattering, so the emitted distribution follows the Chung-Everhart distribution exactly.

Table II gives the energy flux densities into the surface, which is the third moment of the distribution $Q_s^+ = \frac{1}{2}m_s \int_0^\infty v_x^3 f_s(v_x) dv^3$. The clean case has higher ion fluxes and lower electron fluxes into the surface due to the classical profile. However, the increase in electron flux with increased emission is not balanced by the decrease in ion flux. While the oxidized cases both have their ion energy flux decrease by about 40 – 50% compared to the clean cases, the electron flux more than doubles in the marginally collisional case, and more than quadruples in the highly collisional case. Factoring in that the electron energy flux density was higher than the ion flux density even in the classical case, the result is a drastic increase in the total energy flux density for the oxidized cases that more than outweighs the decreases in ion flux multiple times over. While both oxidized cases experience higher energy fluxes than the clean case, the high levels of electron trapping and mixing associated with the turbulence appear to reduce the total energy flux compared to the highly collisional case despite comparable wall potentials.

Case	\tilde{v}_0	$\tilde{\phi}_w$	δ_{tot}	γ	Q_{tot}^+ (W/m ²)	Q_e^+ (W/m ²)	Q_i^+ (W/m ²)
1	0.2	-2.58	0.45	0.45	6.14×10^4	5.49×10^4	6.54×10^3
2	0.2	-1.18	0.99	11.0	2.38×10^5	2.34×10^5	3.94×10^3
3	0.02	-1.18	0.98	8.4	1.29×10^5	1.26×10^5	3.18×10^3

TABLE II. Simulation case results. Normalized collision frequency and wall potential ($\tilde{\phi}_w = q_0 \phi_w / T_0$), emission coefficients, and energy density fluxes are given.

The values $\gamma > 1$ for the oxidized cases suggest the potential for a transition to an inverse sheath in the presence of ion-neutral effects.¹⁴ If this does indeed happen, it is expected that the trend of increasing electron flux and decreasing ion flux will occur at even greater scales.

V. CONCLUSION

The addition of oxidation and impurities to a lithium surface drastically alters its interactions with a plasma, increasing the surface emission significantly and causing the sheath to take on an SCL profile. The result is increased total energy flux into the wall.

While this work gives insight into what is occurring at the wall, some natural extensions of the work require additional considerations. The most obvious omission highlighted by previous discussion was that of ion-neutral effects, which have the potential to trigger an even more dramatic reversal in sheath behavior through the transition to an inverse sheath.

The question of how the emission might impact the edge plasma is left open by this work. In these simulations, the source region was fixed and magnetic fields are neglected. In actual fusion devices, the presence of magnetic fields would add grazing angle effects, requiring at least a second velocity space dimension and an angle-dependent treatment of the emission. The angle is easily accounted for in the emission algorithms,¹⁸ but increase in computational cost for each additional dimension required is significant. To fully gauge possible effects on plasma performance, better inflow mechanisms at the presheath edge which sustain the sheath without enforcing a steady, smooth condition are necessary.

Regardless of these limitations, the increase in emissivity with lithium oxidation justifies further examination into what precautions are necessary to maximize the benefits of employing lithium walls in the confinement of plasmas.

ACKNOWLEDGMENTS

The work presented here was supported by the U.S. Department of Energy ARPA-E BETHE program under Grant No. DE-AR0001263, and by the NSF Collaborative Research: Frameworks: A Software Ecosystem for Plasma Science and Space Weather Applications project under Award Number 2209471.

The simulations presented in this article were performed on computational resources managed and supported by Princeton Research Computing, a consortium of groups including

the Princeton Institute for Computational Science and Engineering (PICSciE) and the Office of Information Technology's High Performance Computing Center and Visualization Laboratory at Princeton University.

DATA AVAILABILITY STATEMENT

All the simulation results presented in this paper were produced by and are reproducible using the open-source Gkeyll software. Information for obtaining, installing, and running Gkeyll may be found on the documentation site.¹⁹ The input files for the simulations used to produce the results in this paper may be acquired from the repository at https://github.com/ammahakim/gkyl-paper-inp/tree/master/2025_PoP_LithiumSheath.

- ¹L. Artsimovich, "Tokamak devices," *Nuclear Fusion* **12**, 215 (1972).
- ²D. M. Goebel and I. Katz, *Fundamentals of electric propulsion: ion and Hall thrusters* (John Wiley & Sons, Ltd, 2008).
- ³S. Robertson, "Sheaths in laboratory and space plasmas," *Plasma Physics and Controlled Fusion* **55**, 093001 (2013).
- ⁴G. D. Hobbs and J. A. Wesson, "Heat flow through a langmuir sheath in the presence of electron emission," *Plasma Physics* **9**, 85 (1967).
- ⁵R. Majeski, L. Berzak, T. Gray, R. Kaita, T. Kozub, F. Levinton, D. Lundberg, J. Manickam, G. Pereverzev, K. Snieckus, *et al.*, "Performance projections for the lithium tokamak experiment (Itx)," *Nuclear Fusion* **49**, 055014 (2009).
- ⁶R. Majeski, H. Kugel, R. Kaita, S. Avsarala, M. Bell, R. Bell, L. Berzak, P. Beiersdorfer, S. Gerhardt, E. Granstedt, *et al.*, "The impact of lithium wall coatings on nstx discharges and the engineering of the lithium tokamak experiment (Itx)," *Fusion engineering and design* **85**, 1283–1289 (2010).
- ⁷H. Kugel, J. Allain, M. Bell, R. Bell, A. Diallo, R. Ellis, S. Gerhardt, B. Heim, M. Jaworski, R. Kaita, *et al.*, "Nstx plasma operation with a liquid lithium divertor," *Fusion Engineering and Design* **87**, 1724–1731 (2012).
- ⁸A. De Castro, C. Moynihan, S. Stemmley, M. Szott, and D. Ruzic, "Lithium, a path to make fusion energy affordable," *Physics of Plasmas* **28** (2021).
- ⁹A. Zakharov, A. Gorodetsky, V. K. Alimov, S. Kanashenko, and A. Markin, "Hydrogen retention in plasma-facing materials and its consequences on tokamak operation," *Journal of nuclear materials* **241**, 52–67 (1997).
- ¹⁰H. Bruining and J. De Boer, "Secondary electron emission: Part i. secondary electron emission of metals," *Physica* **5**, 17–30 (1938).
- ¹¹A. Capece, M. Patino, Y. Raiteses, and B. Koel, "Secondary electron emission from lithium and lithium compounds," *Applied Physics Letters* **109** (2016).
- ¹²C. Skinner, R. Sullenberger, B. E. Koel, M. Jaworski, and H. Kugel, "Plasma facing surface composition during nstx li experiments," *Journal of Nuclear Materials* **438**, S647–S650 (2013).
- ¹³M. D. Campanell, "Negative plasma potential relative to electron-emitting surfaces," *Phys. Rev. E* **88**, 033103 (2013).
- ¹⁴M. D. Campanell and M. V. Umansky, "Strongly emitting surfaces unable to float below plasma potential," *Phys. Rev. Lett.* **116**, 085003 (2016).
- ¹⁵M. D. Campanell and M. Umansky, "Are two plasma equilibrium states possible when the emission coefficient exceeds unity?" *Physics of Plasmas* **24** (2017).
- ¹⁶P. Cagas, A. Hakim, J. Juno, and B. Srinivasan, "Continuum kinetic and multi-fluid simulations of classical sheaths," *Physics of Plasmas* **24**, 022118 (2017), <https://doi.org/10.1063/1.4976544>.
- ¹⁷C. R. Skolar, K. Bradshaw, J. Juno, and B. Srinivasan, "Continuum kinetic investigation of the impact of bias potentials in the current saturation regime on sheath formation," *Physics of Plasmas* **30** (2023).
- ¹⁸K. Bradshaw and B. Srinivasan, "Energy-dependent implementation of secondary electron emission models in continuum kinetic sheath simulations," *Plasma Sources Science and Technology* **33**, 035008 (2024).
- ¹⁹Gkeyll, (2024), <https://gkeyll.readthedocs.io>.
- ²⁰B. Cockburn and C.-W. Shu, "Runge–kutta discontinuous galerkin methods for convection-dominated problems," *Journal of Scientific Computing* **16**, 173–261 (2001).
- ²¹J. Juno, A. Hakim, J. TenBarge, E. Shi, and W. Dorland, "Discontinuous galerkin algorithms for fully kinetic plasmas," *Journal of Computational Physics* **353**, 110–147 (2018).
- ²²A. Hakim and J. Juno, "Alias-free, matrix-free, and quadrature-free discontinuous galerkin algorithms for (plasma) kinetic equations," in *SC20: International Conference for High Performance Computing, Networking, Storage and Analysis* (IEEE, 2020) pp. 1–15.
- ²³Y. Li, B. Srinivasan, Y. Zhang, and X.-Z. Tang, "Bohm criterion of plasma sheaths away from asymptotic limits," *Physical Review Letters* **128**, 085002 (2022).
- ²⁴Y. Li, B. Srinivasan, Y. Zhang, and X.-Z. Tang, "Transport physics dependence of bohm speed in presheath–sheath transition," *Physics of Plasmas* **29** (2022).
- ²⁵R. J. Procassini, C. K. Birdsall, and E. C. Morse, "A fully kinetic, self-consistent particle simulation model of the collisionless plasma-sheath region," *Physics of Fluids B* **2** (1990), 10.1063/1.859229.
- ²⁶K. Jensen, *Introduction to the Physics of Electron Emission* (John Wiley & Sons, Inc, New Jersey, 2018) pp. 155–161.
- ²⁷M. A. Furman and M. T. F. Pivi, "Probabilistic model for the simulation of secondary electron emission," *Phys. Rev. ST Accel. Beams* **5**, 124404 (2002).
- ²⁸R. Cimino, I. R. Collins, M. A. Furman, M. Pivi, F. Ruggiero, G. Rumolo, and F. Zimmermann, "Can low-energy electrons affect high-energy physics accelerators?" *Phys. Rev. Lett.* **93**, 014801 (2004).
- ²⁹R. Larciprete, D. R. Grosso, M. Commisso, R. Flammini, and R. Cimino, "Secondary electron yield of cu technical surfaces: Dependence on electron irradiation," *Phys. Rev. ST Accel. Beams* **16**, 011002 (2013).
- ³⁰A. Andronov, A. Smirnov, I. Kaganovich, E. Startsev, Y. Raiteses, and V. Demidov, "Secondary electron emission yield in the limit of low electron energy," arXiv preprint arXiv:1309.4658 (2013).
- ³¹R. Cimino, L. A. Gonzalez, R. Larciprete, A. Di Gaspare, G. Iadarola, and G. Rumolo, "Detailed investigation of the low energy secondary electron yield of technical cu and its relevance for the lhc," *Phys. Rev. ST Accel. Beams* **18**, 051002 (2015).
- ³²I. Bronshtein and V. Roshchin, "Reflection of electrons and secondary electron emission from some metal surfaces at low primary electron energy," *Sov. J. Tech.-Phys.* 2271 (1958).
- ³³I. Khan, J. Hobson, and R. Armstrong, "Reflection and diffraction of slow electrons from single crystals of tungsten," *Physical Review* **129**, 1513 (1963).
- ³⁴Z. Yakubova and N. Gorbatiy, "Reflection of slow electrons from the (110) face of a tungsten crystal," *Soviet Physics Journal* **13**, 1477–1482 (1970).
- ³⁵J. Cazaux, "Reflectivity of very low energy electrons (< 10 eV) from solid surfaces: Physical and instrumental aspects," *Journal of Applied Physics* **111** (2012).
- ³⁶T. Everhart, "Simple theory concerning the reflection of electrons from solids," *Journal of Applied Physics* **31**, 1483–1490 (1960).
- ³⁷K. Bradshaw, *Emitting Wall Boundary Conditions in Continuum Kinetic Simulations: Unlocking the Effects of Energy-Dependent Material Emission on the Plasma Sheath*, Phd thesis, Virginia Polytechnic Institute and State University, Blacksburg, VA (2024), available at <https://vtechworks.lib.vt.edu/handle/10919/118137>.
- ³⁸M. Chung and T. Everhart, "Simple calculation of energy distribution of low-energy secondary electrons emitted from metals under electron bombardment," *Journal of Applied Physics* **45**, 707–709 (1974).
- ³⁹W. M. Haynes, *CRC handbook of chemistry and physics* (CRC press, 2016).